

Technical Articles

- Analysis of Fuel Vapour Bubble Dilution Dynamics and In-Vessel Actinide Transport under Severe Accident Scenario in SFR
- Thermodynamic Modeling of Uranyl Nitrate and Nitric Acid Distribution Coefficient in TiAP-HNO₃ system

Young Officer's Forum

- Optimization of Spatial Light Modulator to Generate Aberration Free Holographic Optical Traps

Young Researcher's Forum

- Magnetic Domain Structure and its Field Induced Dynamics in Polycrystalline Pure Iron and Steels Studied using Magnetic Force Microscopy

News and Events

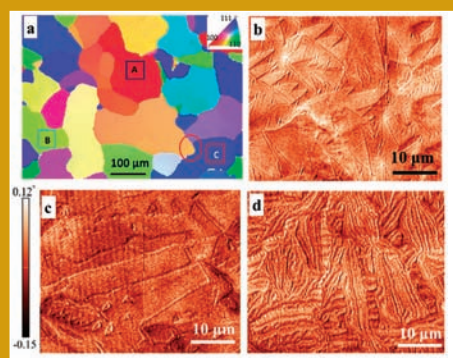
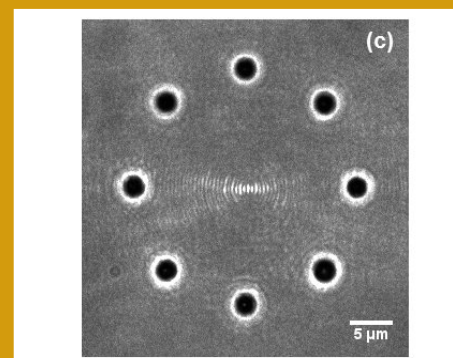
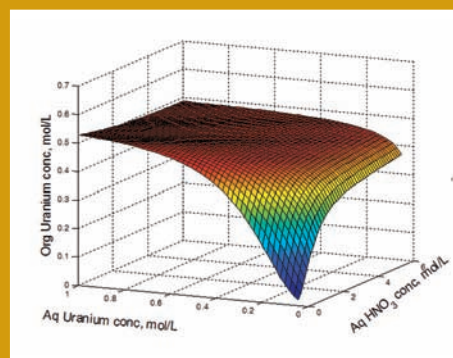
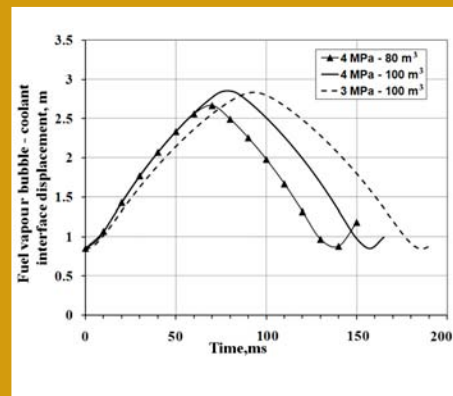
- Foundation Day Celebration of IGCAR

Conference and Meeting Highlights

- Dr. Baldev Raj Memorial Bridge Course on Non-destructive Evaluation and Quality Assurance (BRM-BCNQ)
- One day Training Program on "Nuclear Radiation in Fuel Cycle"

HBNI-IGCAR Corner

Awards & Honours



From the Editorial Committee

Dear Reader,

It is our pleasant privilege to forward a copy of the latest issue of IGC Newsletter (Volume 121, July 2019 issue).

In the first technical article Dr. P. Mangarjuna Rao & colleagues from Safety Engineering Division, FRTG have discussed about the Analysis of Fuel Vapour Bubble Dilation Dynamics and In-Vessel Actinide Transport under Severe Accident Scenario in Sodium cooled Fast spectrum Reactors (SFR).

In the second technical article Shri S. Balasubramonian and colleagues from Reprocessing Group have discussed about the Thermodynamic Modeling of Uranyl Nitrate and Nitric Acid Distribution Coefficient in TiAP-HNO₃ system.

This issue's Young Officer's Forum features an article by Dr. Deepak Kumar Gupta from Materials Science Group (MSG) discussing about the Optimization of Spatial Light Modulator to Generate Aberration Free Holographic Optical Traps.

Dr. J Abuthahir has described about Magnetic Domain Structure and its Field Induced Dynamics in Polycrystalline Pure Iron and Steels studied using Magnetic Force Microscopy in the Young Researcher's Forum.

We are happy to share with you the awards, honours and distinctions earned by our colleagues.

We look forward to your comments, continued guidance and support.

With best wishes and personal regards

Editorial Committee, IGC Newsletter

Analysis of Fuel Vapour Bubble Dilation Dynamics and In-Vessel Actinide Transport under Severe Accident Scenario in SFR

In pool type Sodium cooled Fast spectrum Reactors (SFR), the core is kept permanently submerged in the liquid sodium pool. The fuel ($UO_2 + PuO_2$ mixture) in SFR core is kept inside the hermitically sealed stainless steel tubes. A sustained Power Coolant Mismatch (PCM) due to Anticipated Transient Without Scram (ATWS) could result in coolant boiling, core material (fuel and stainless steel) melting and relocation. In case of prompt neutronic recriticality under the new core configuration, rapid dispersion of core materials (\sim few hundred milliseconds) takes place and the phenomenon is termed as energetic Core Disruptive accident (CDA). Several inherent shutdown mechanisms make it a highly unlikely event and therefore energetic CDA is generally considered as the bounding phenomenon for the safety analysis of ATWS in SFR. In this regard, a parametric analysis is carried out to understand the expansion behavior of fuel vapour bubble and the associated actinide release and transport from the disrupted core to liquid sodium pool under the energetic CDA conditions.

Energetic CDA and Material Dispersion from the Disrupted Core

The prompt neutronic criticality during the CDA resultant extensive core material relocation, terminates with the formation of high temperature high pressure zone, known as fuel vapour bubble. The fuel vapour bubble is not in equilibrium with the surrounding and expands into the overhead liquid sodium pool resulting in the

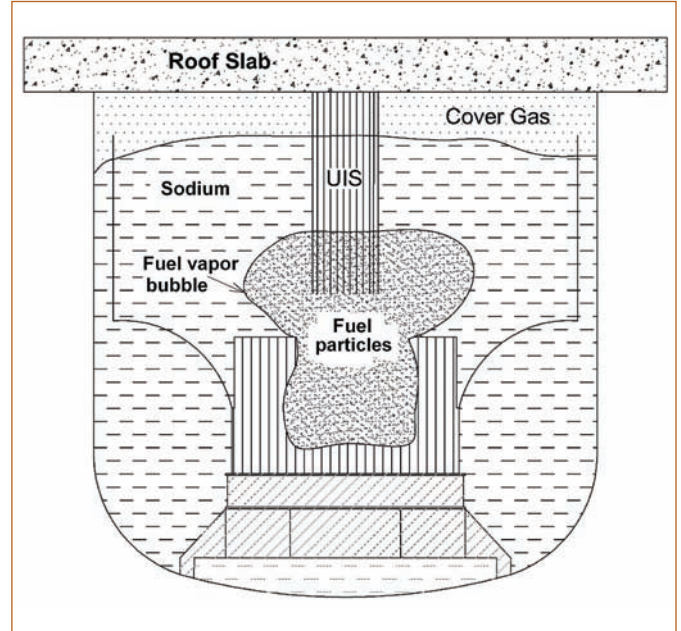


Figure 1: Schematic of fuel vapour bubble evolution during CDA in a pool type SFR (UIS = Upper Internal Structure)

oscillation of the bubble. The expanding fuel vapour bubble mostly consists of fuel vapour along with fragmented fuel particles and solid fission products with low volatility. The transfer of fuel particles from the disrupted core due to energetic CDA is an important consideration in the radiological consequence assessment of energetic CDA. Figure 1 shows the schematic of fuel vapour bubble evolution during energetic CDA.

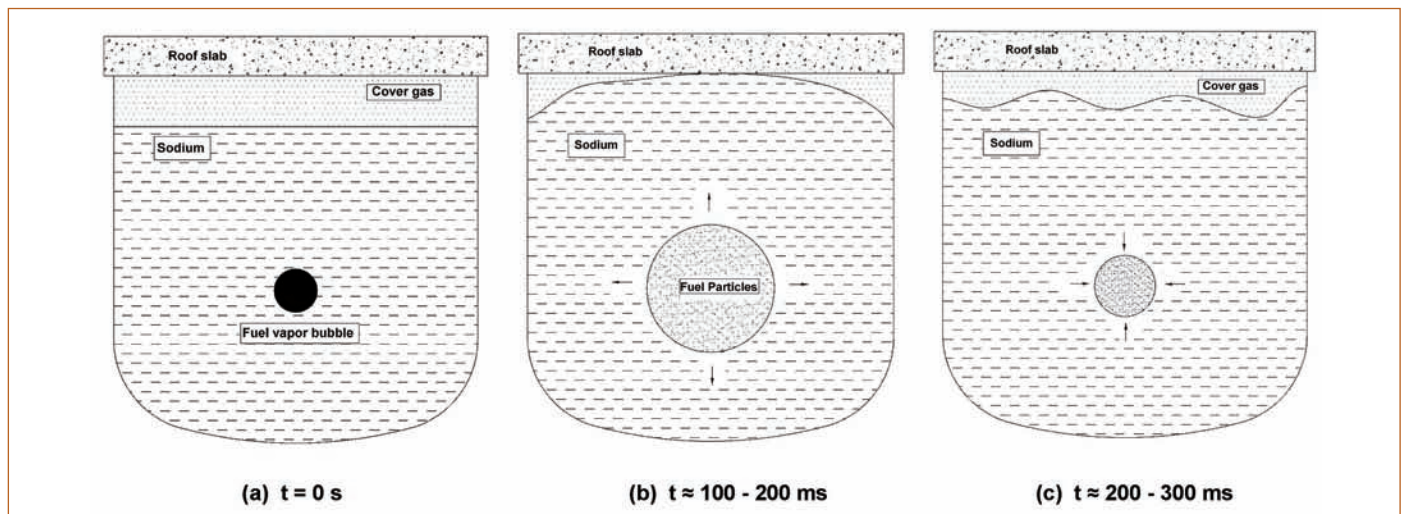


Figure 2: Schematic of fuel vapour bubble expansion under idealized condition. (a) Initial condition, (b) Expansion in to liquid sodium pool, (c) Compression of fuel vapour bubble

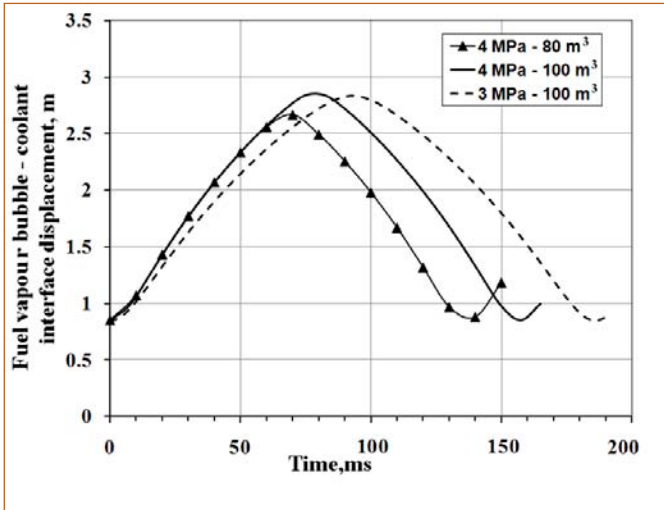


Figure 3: Fuel vapour bubble - coolant interface displacement as a function of initial bubble pressure and cover gas volume

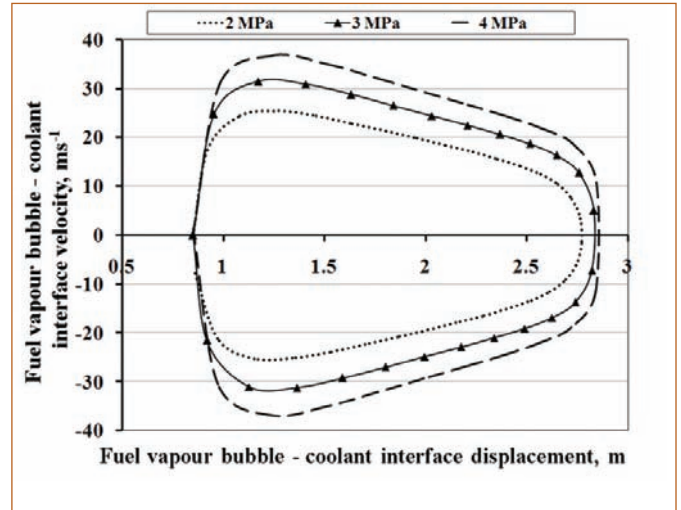


Figure 4: Phase portrait of bubble oscillation for various initial bubble pressures

The evolution of fuel vapour bubble inside the sodium pool is influenced by the internal structures of reactor. In the present analysis the bubble is assumed to undergo unrestrained expansion and the presence of internal structures in the reactor is ignored. Similarly, Lagrangian trajectories of fuel particles are evaluated by assuming dilute flow regime. The results would serve as a benchmark data for further detailed analysis. Figure 2 shows the schematic of the geometry considered along with expansion and compression of the fuel vapour bubble under idealised condition.

The in-house computer code PTRACK has been modified to account for unrestrained expansion of fuel vapour bubble in the sodium pool. The code consists of two modules namely, fluid

module and particle module. The fluid module evaluates the instantaneous local fuel vapour velocity corresponding to the fuel particle position and it is given as input to evaluate the fuel particle trajectories in particle module (i.e., one way coupling).

Fuel Vapour Bubble Expansion and Lagrangian Particle Trajectories

The fuel vapour bubble expansion is a short term phenomenon (~ few hundred milliseconds) wherein buoyancy and heat transfer effects are ignored in the present analysis. The initial volume and pressure of the fuel vapour bubble are given as input conditions and the molten fuel is assumed to be in saturated

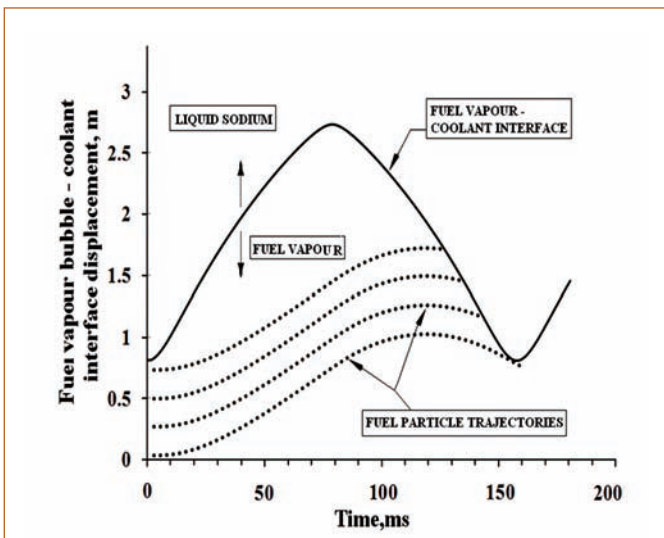


Figure 5: Fuel particle trajectories inside the expanding fuel vapour bubble. (Initial bubble pressure = 4 MPa, Particle diameter = 300 micron)

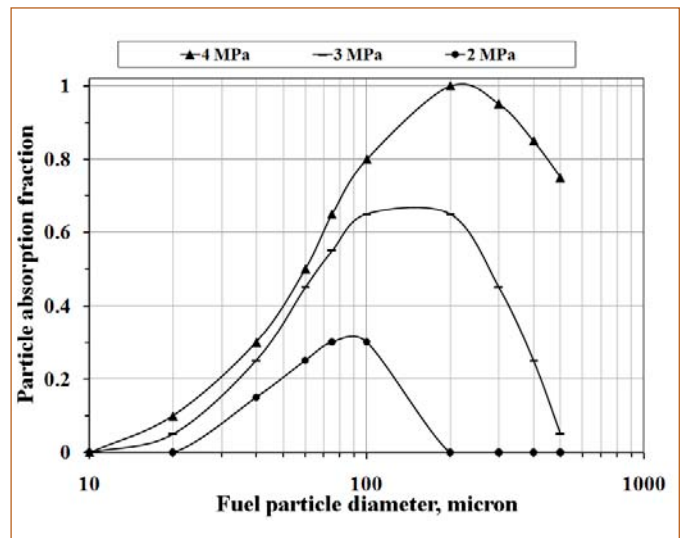


Figure 6: Variation of particle absorption fraction with particle diameter and initial bubble pressure

liquid state. The expansion of fuel vapour bubble in the sodium pool causes compression in cover gas space. When the cover gas pressure attains a maximum value, the cover gas starts expanding by compressing the fuel vapour bubble, resulting in oscillation of bubble-coolant interface. The instantaneous bubble and cover gas pressures are calculated using reversible adiabatic expansion equations.

During the course of fuel vapour bubble expansion, phenomena such as fuel vapour condensation, hydrodynamic fragmentation, fuel coolant interaction results in an initial particle size spectrum covering submicron particle to large particles ($> 100\mu\text{m}$). In the present work, particle trajectories inside an expanding fuel vapour bubble are evaluated by solving Particle Momentum Equation (PME). The PME is based on Newton's second law of motion and quantifies all the forces acting on the particle.

Parametric Analysis and Results

The analysis has been carried out to evaluate bubble-coolant interface displacement with initial fuel vapour bubble pressure and initial cover gas volume as parameters. The initial fuel vapour bubble pressures are 2, 3 and 4 MPa with the initial spherical bubble volume of 2.57 m^3 . For cover gas space, the initial pressure is 0.1 MPa with the initial volumes of 80 and 100 m^3 . Since the bubble expansion process time scale is in the order of a few hundred milliseconds, the present analysis is carried out for the duration of 500 ms.

Figure 3 shows the bubble-coolant interface displacement for initial pressures of 4 and 3 MPa. Analysis of results have shown that the oscillation time period for initial pressures of 4, 3 and 2 MPa are 138 ms, 184 ms and 230 ms respectively for the initial

cover gas volume of 100 m^3 . Also the oscillation time period decreases with the decrease in initial cover gas volume. The phase portraits of bubble oscillation for initial bubble pressures of 2, 3 and 4 MPa with 100 m^3 initial cover gas volume are given in Figure. 4.

Particle trajectories are obtained by solving the one-dimensional PME for the given initial bubble pressure and particle diameter. The particles are assumed to be uniformly distributed inside the fuel vapour bubble. The particles are assumed to be permanently absorbed by the sodium pool once they cross bubble-coolant interface. The behavior of fuel particles is quantified by using Particle Absorption Fraction, defined as the ratio between the number of particles absorbed by sodium pool and the initial number of particles in the bubble.

The evaluated oscillation of bubble-coolant interface and the associated trajectories of arbitrarily chosen four particles of 300 micron with an initial bubble pressure of 4 MPa is shown in Figure 5. Figure 6 shows the variation of particle absorption fraction with particle diameter from 10 micron to 500 micron for various initial bubble pressures.

Results show that fuel particles with diameter ranging from few tens of microns to few hundreds of microns are effectively removed from the fuel vapour bubble by virtue of particle inertia and retained by the sodium pool and not expected to contribute to the radiological source term.

*Reported by
P. Mangarjuna Rao & colleagues
Safety Engineering Division/FRTG*

Thermodynamic Modeling of Uranyl Nitrate and Nitric Acid Distribution Coefficient in TiAP-HNO₃ system

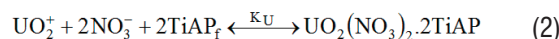
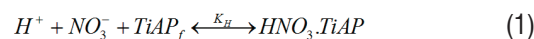
Triisoamyl phosphate (TiAP) is a potential alternate solvent to Tributyl phosphate (TBP) for the separation of uranium and plutonium from the spent nuclear fuel using the PUREX process. TiAP has the advantage of lower aqueous solubility, high extraction power and high third phase formation limit for plutonium as compared to TBP. These advantages are favorable for using TiAP for processing of fast reactor spent fuels which contains high plutonium concentration. In order to get favorable hydrodynamic properties (density and viscosity) and optimum decontamination factor, TiAP must be diluted with suitable diluents usually n-dodecane. Generally 1.1 M TiAP in n-dodecane (n-DD), (i.e.) 36 vol.% was found to be suitable for reprocessing application. Large amount of equilibrium data were reported for the extraction of uranium and plutonium by 1.1 M TiAP. These data can be used for the mathematical modeling of the solvent extraction equilibrium. The mathematical description of solvent extraction equilibrium is required for the design & optimization of the flowsheet and process control. Therefore, the accurate prediction of the concentration of metal ions in the extracted organic phase is important. Hence the mathematical description of the solvent extraction equilibria must be accurate enough to predict the concentration profiles. The extraction of various components by solvent in the organic phase is usually described by assuming a specific set of species with predefined stoichiometric coefficients in the organic phase. The equilibrium constant for the formation of these species are treated as adjustable parameter and estimated through least square criterion which best fits the experimental data. During the modeling of solvent extraction equilibrium using the law of mass action, the activity coefficient can be assumed as unity or can be described through suitable activity coefficient model. The inclusion of activity coefficient improves the accuracy of the prediction of the model. This also enables the interpolation and extrapolation of the experimental data.

Experimental procedure

The organic phase (1.1 M TiAP in n-DD) was initially equilibrated with nitric acid of required concentration. After phase separation the organic phase was equilibrated with equal volumes of uranyl nitrate solutions for 30 mins at 303 K and allowed to settle. Suitable aliquots were then withdrawn from each phase and concentration of U(VI) were determined.

Modeling of Solvent extraction equilibrium

During solvent extraction, the organic phase (1.1 M TiAP in n-DD) extracts uranyl nitrate, nitric acid and water. The extraction equilibria of nitric acid and uranyl nitrate can be described as



The law of mass action states that the rate of chemical reaction is proportional to the ratio of activity of products to activity of reactants which defines the equilibrium constant for nitric acid (K_H) and uranyl nitrate extraction (K_U) as follows

$$K_H = \frac{a_{HNO_3 \cdot TiAP}}{a_{HNO_3} a_{TiAP_f}} \quad (3)$$

$$K_U = \frac{a_{UO_2(NO_3)_2 \cdot 2TiAP}}{a_{UO_2(NO_3)_2} a_{TiAP_f}^2} \quad (4)$$

The activity of nitric acid (a_{HNO_3}) and uranyl nitrate ($a_{UO_2(NO_3)_2}$) in the aqueous phase were estimated from their molar activity coefficient and molar concentration. The activity of complexes and free TiAP ($TiAP_f$) in the organic phase is equal to its concentration since the activity coefficient in the organic phase was assumed as unity.

The concentration of uranyl nitrate and nitric acid in the organic phase was estimated from equations 3 and 4. The free TiAP concentration in the organic phase is estimated by solving the mole balance equation formed by equating the concentration of free TiAP and complexed TiAP to the initial concentration (1.1 M).

Aqueous phase non ideality

The activity coefficient of species in the aqueous phase can be estimated from one of several electrolyte activity coefficient models. The choice of the activity coefficient model is based on the concentration range and nature of mixed electrolyte/s present in the solution. In this work, electrolyte Non Random Two liquid model (eNRTL) is adopted, which is a semi theoretical model based on local composition concept which can predict the activity coefficient accurately up to very high concentration. In the eNRTL model the excess Gibbs free energy is expressed as the sum of two contributions resulting from long range electrostatic forces between ions and short range forces between all the components present in the solution. The long range electrostatic contribution is

accounted by the extended form of the Debye-Huckel equation. The short range contribution is accounted using the local composition concept. This is based on the assumption of like-ion repulsion and electro neutrality. It is assumed that the local composition of cation around cation is zero (similarly for anions around anion) which is equivalent to assuming that the repulsive forces between like charged ions are extremely large. The electro neutrality assumption states that the distribution of cations and anions around the central solvent molecule is such that the net local ionic charge is zero. Based on the above assumptions the excess Gibbs free energy is derived and the activity coefficients of solvent, cations and anion were obtained by differentiating the excess Gibbs free energy with their respective number of moles. In the activity coefficient expression, the interaction energies between electrolyte (ca) and solvent (m) are denoted as $\tau_{ca,m}$ and $\tau_{m,ca}$ and are usually called as the binary interaction parameters which must be determined from experimental water activity data.

Organic phase non ideality

The interaction that exists in the organic phase such as hydrogen bonding and dipole-dipole interaction were weak as compared to the electrostatic interaction in the aqueous phase. Hence the organic phase non ideality is simple as compared to the aqueous phase non ideality. The organic phase non ideality primarily results from the formation of complexes in the organic phase. Thus the equilibrium constant for the formation of the complexes in the organic phase is sufficient to capture the non ideality. The activity coefficient in the organic phase is assumed to be unity.

Modeling of uranyl nitrate and nitric acid extraction

The activity coefficient in the aqueous phase was estimated using original eNRTL model using the mole fraction scale. Hence the molarity scale used in the experiments was converted to mole fraction scale using the solution density that was estimated from the reported density relationship. The available experimental water activity data of HNO₃-H₂O and UO₂(NO₃)₂-H₂O binary systems and their ternary system were used for the estimation of interaction parameters in the eNRTL model. In addition to water activity data, the nitric acid partial pressure data reported for the ternary system was also included for the estimation of eNRTL interaction parameters. The parameter estimation was performed using MATLAB optimization routine by minimizing the objective function, which is defined as the sum of squared deviation between the experimental and calculated water activity and partial pressure of nitric acid over the HNO₃-UO₂(NO₃)₂-H₂O ternary system. The optimized eNRTL parameters obtained for the simultaneous

description of binary and ternary experimental data are given in Table 1.

Table 1: The optimized eNRTL interaction parameter for HNO ₃ -UO ₂ (NO ₃) ₂ -H ₂ O system		
Component i	Component j	Binary interaction parameter (τ_{ij})
H ₂ O	(H ⁺ , NO ₃ ⁻)	8.940
(H ⁺ , NO ₃ ⁻)	H ₂ O	-4.668
H ₂ O	(UO ₂ ²⁺ , NO ₃ ⁻)	6.822
(UO ₂ ²⁺ , NO ₃ ⁻)	H ₂ O	-4.260
(H ⁺ , NO ₃ ⁻)	(UO ₂ ²⁺ , NO ₃ ⁻)	2.830
(UO ₂ ²⁺ , NO ₃ ⁻)	(H ⁺ , NO ₃ ⁻)	-2.830

An excellent agreement was obtained between the model predicted and experimental water activity data of HNO₃-H₂O system. However the estimated water activity data of UO₂(NO₃)₂-H₂O binary system deviates from the experimental data beyond 2M concentration. This may be due to the parameter estimation procedure where more weightage was given to the ternary data which results in the poor representation of UO₂(NO₃)₂-H₂O binary data. But excellent agreement was obtained between the model predicted and experimental nitric acid partial pressure data of HNO₃-UO₂(NO₃)₂-H₂O ternary system as shown in Figure 1. The Root Mean Square Deviation (RMSD) between the model predicted and experimental nitric acid partial pressure is 0.44%.

The set of species formed during the extraction of nitric acid and uranyl nitrate into 1.1 M TiAP were assumed based on the data

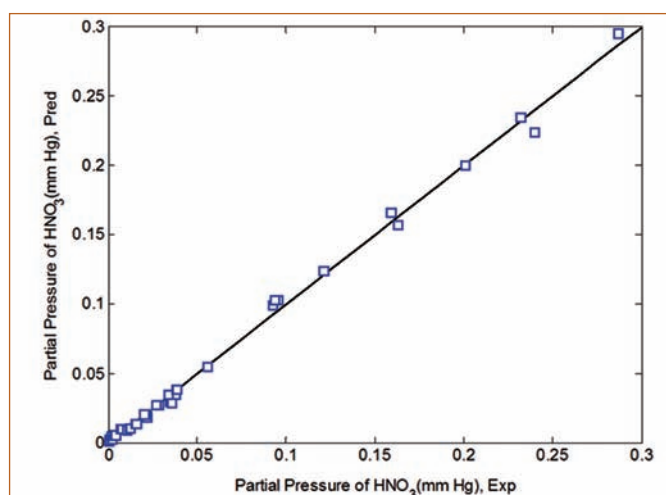


Figure 1: Comparison of experimental and predicted partial pressure of nitric acid over UO₂(NO₃)₂-HNO₃-H₂O system.

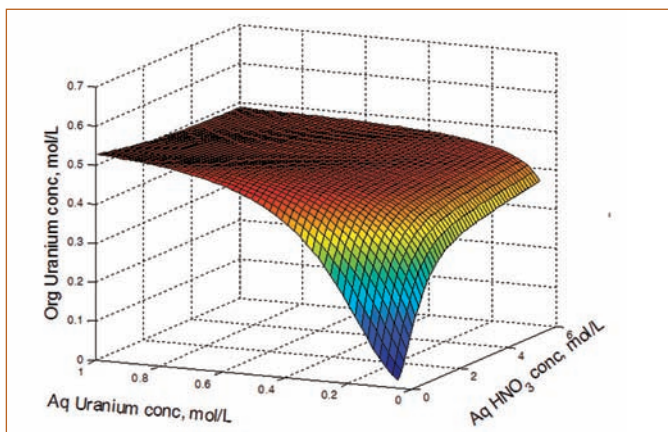


Figure 2: Predicted concentration of uranyl nitrate in organic phase as a function of concentration of nitric acid and uranyl nitrate in aqueous phase.

available in the literature for TBP based system. The species such as $\text{HNO}_3 \cdot \text{TiAP}$, $\text{HNO}_3 \cdot 2\text{TiAP}$, $\text{UO}_2(\text{NO}_3)_2 \cdot 2\text{TiAP}$, $\text{UO}_2(\text{NO}_3)_2 \cdot 3\text{TiAP}$ and $\text{HNO}_3 \cdot \text{UO}_2(\text{NO}_3)_2 \cdot 2\text{TiAP}$ were considered as the most dominant species involved. Since the water present in the organic phase is assumed as the solubilized water, the extraction of water along with the other extractable species in the organic phase was not considered. The equilibrium constant for the formation of these species considered in the organic phase were estimated by minimizing the sum of squared deviation between the experimental and estimated organic phase concentration. The experimental data collected in this work along with the uranyl nitrate extraction data for various aqueous concentrations of nitric acid, reported in the literature was used for the estimation of equilibrium constant/s.

The estimated equilibrium constant for the formation of the species $\text{UO}_2(\text{NO}_3)_2 \cdot 2\text{TiAP}$ and $\text{HNO}_3 \cdot \text{TiAP}$ were 43.99 and 0.505 respectively. The RMSD (%) between the experimental and predicted uranyl nitrate and nitric acid concentration in the organic phase was 1.96 and 3.31% and also the statistical correlation coefficient (R^2) is 0.99 and 0.96 respectively for uranyl nitrate and nitric acid extraction. Figures 2 and 3 show the predicted concentration of

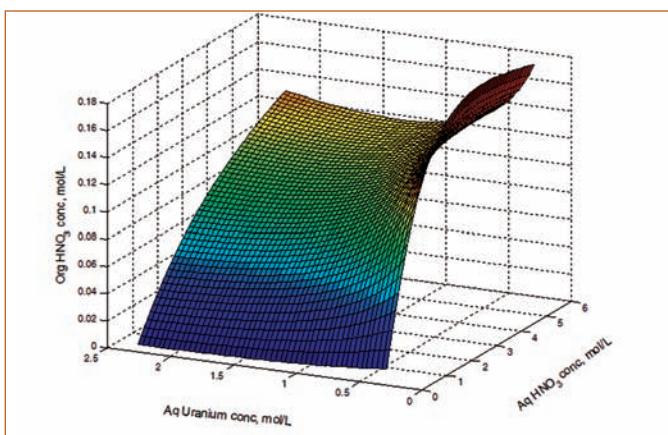


Figure 3: Predicted concentration of nitric acid in organic phase as a function of nitric acid and uranyl nitrate in aqueous phase.

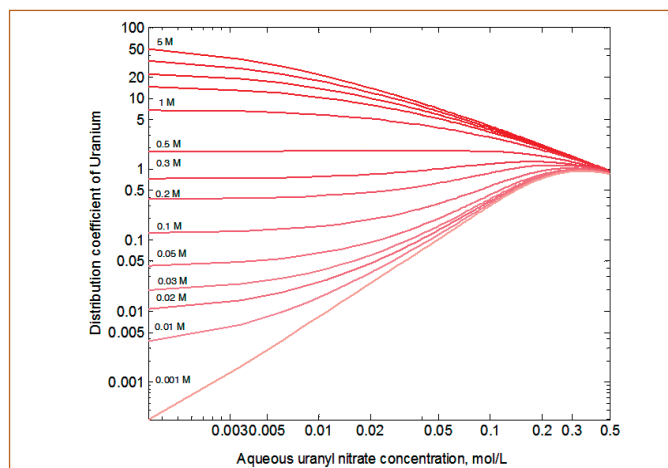


Figure 4: The distribution coefficient of uranium for various aqueous uranyl nitrate and nitric acid concentration.

uranyl nitrate and nitric acid in organic phase as a function of their concentration in aqueous phase. The distribution coefficient of uranium as a function of various concentrations of uranyl nitrate and nitric acid in the aqueous phase is shown in Figure 4. At high aqueous phase concentrations of uranyl nitrate, good agreement was obtained between the experimental and predicted organic phase concentration as compared to the lower concentration region. The predicted concentration of nitric acid agrees well with the experimental data below 4M aqueous concentration of nitric acid. Beyond this the predicted concentration of nitric acid is lower than the experimental value. To improve the accuracy of fitting, the following species $\text{UO}_2(\text{NO}_3)_2 \cdot 3\text{TiAP}$ and $\text{HNO}_3 \cdot 2\text{TiAP}$ were included in the optimization routine. But this did not improve the fit significantly. Hence it may be assumed that the higher order TiAP species may form only in the higher concentration of free TiAP in the organic phase. However the inclusion of $\text{HNO}_3 \cdot \text{UO}_2(\text{NO}_3)_2 \cdot 2\text{TiAP}$ species marginally improved the accuracy of the prediction of the concentration of nitric acid in the organic phase especially in the high concentration region of nitric acid. During the extraction of uranyl nitrate from higher concentration of nitric acid, the competition between the extraction of nitric acid and uranyl nitrate might lead to the formation of $\text{HNO}_3 \cdot \text{UO}_2(\text{NO}_3)_2 \cdot 2\text{TiAP}$ species where nitric acid is co-extracted with the $\text{UO}_2(\text{NO}_3)_2 \cdot 2\text{TiAP}$ species. Though the inclusion of $\text{HNO}_3 \cdot \text{UO}_2(\text{NO}_3)_2 \cdot 2\text{TiAP}$ species marginally improved the prediction of nitric acid profile with the estimated equilibrium constant of 0.015, it did not improve the accuracy of prediction in the case of uranyl nitrate extraction. Hence the $\text{HNO}_3 \cdot \text{TiAP}$ and $\text{UO}_2(\text{NO}_3)_2 \cdot 2\text{TiAP}$ species were sufficient for satisfactory prediction of the extraction behaviour of uranyl nitrate and nitric acid by 1.1 M TiAP in dodecane.

Reported by

S. Balasubramonian & colleagues
Reprocessing Group.

Young Officer's FORUM

Optimization of Spatial Light Modulator to Generate Aberration Free Holographic Optical Traps

An optical tweezer is a tightly focused laser beam capable of holding and moving microscopic objects. It has become an indispensable, non-destructive tool for manipulation of different microscopic objects since 1986. Because of the ability of non-invasive probing at the mesoscopic scale and manipulation capability with nanometer accuracy, optical tweezers find applications in various fields of research, such as the study of particle interactions in complicated geometries, hydrodynamic interactions between colloidal spheres, optical binding, colloidal transport, optical sorting, etc. However many applications require control of a multitude of particles, like manipulating them in real time and placing them in definite positions with desired symmetry. Holographic Optical Tweezers (HOTs) play an important role, allowing for the creation of multiple optical spots in real time. HOTs uses the technique of beam shaping combined with digital holography accomplished by a phase-only spatial light modulator (SLM). A HOTs set-up is designed and developed by the use of a spatial light modulator as a beam shaper. The HOTs setup is developed with an aim to create an array of trap spots to trap multitude sets of particles in their desired positions. The technique of HOTs requires efficient and uniform distribution of light among the desired spots, free from aberrations, to efficiently trap the particles in them.



Dr. Deepak Kumar Gupta is working as a Scientific Officer in Light Scattering Studies Section (LSSS) of Materials Science Group (MSG). He is from 3rd batch of BARC training School at IGCAR campus and joined the group in

2009. He is the Homi Bhabha award winner in the Training School from the Materials Science discipline. He obtained his M.Sc. in Physics from Sambalpur University, Odisha. He is the University Gold Medal winner for becoming topper in M.Sc. and Dillip Kumar Pati Gold medal winner for the best postgraduate regular student. He obtained his Ph.D. in physical sciences from Homi Bhabha National Institute for the thesis titled "Design and Development of Holographic Optical tweezers and Studies on Colloidal Systems". His current area of interest comprises studies related to holographic optical trapping and its applications in the area of soft condensed matter and biological sciences.

In general, liquid-crystal-based SLMs show their inherent non-linear phase response as a function of addressed gray values, which limits their performance in some of their applications. A diffraction-based technique is employed to characterize and calibrate the SLM. A methodology to optimize the graphics card properties and calibrate the SLM, correcting its nonlinear phase response behavior is presented. A LUT is generated and the SLM is optimized for its maximum attainable phase modulation depth and maximum diffraction efficiency. In addition to the non-linearity in the phase response, these liquid-crystal-based modulators show different phase responses in the different spatial regions of the SLM, which may be due to the thickness variations across the active area of SLM. The Spatially Varying Phase Response (SVPR) may arise due to differential liquid crystal heating due to variation in power over the active area because of the spatial profile of the incident laser. In this work, a simple and robust method to calibrate an SLM suffering from a SVPR is presented.

HOTs set-up

A HOTs set-up is designed and developed, which employs a phase-only reflective SLM as the programmable diffraction device. The SLM consists of parallel aligned nematic liquid crystal molecules

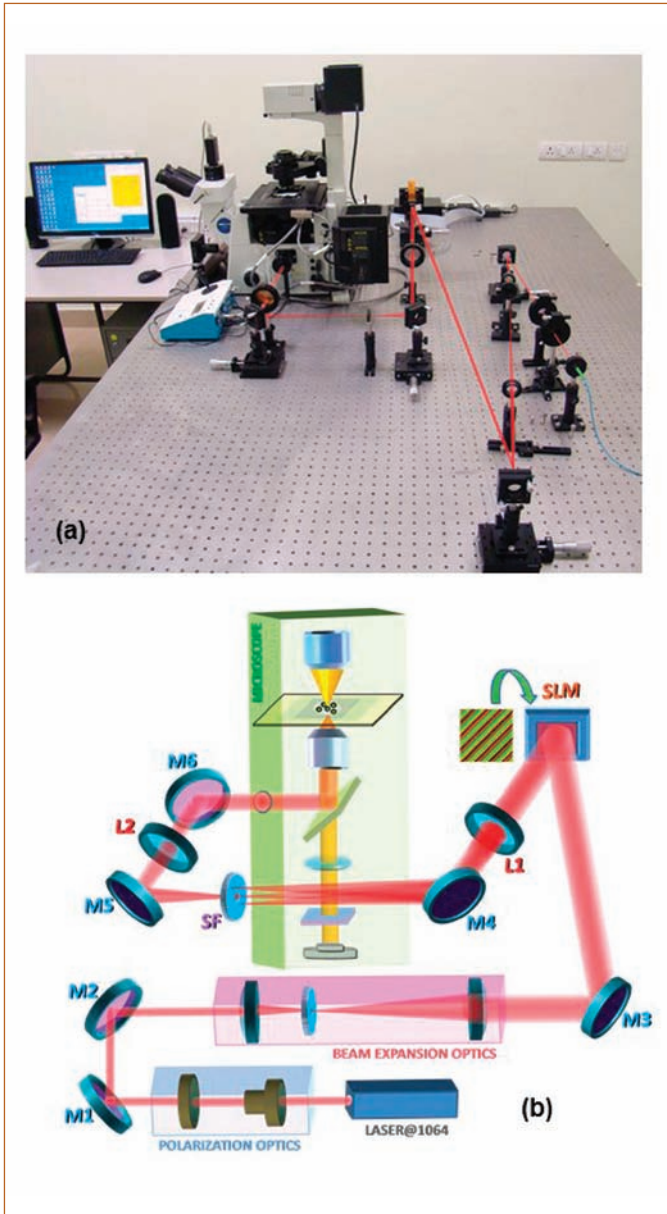


Figure 1: (a) Photograph of the HOTS set-up. (b) Schematics of the HOTS setup.

sandwiched between a pixelated back electrode and a transparent front electrode. Each pixel can be independently controlled, allowing simultaneous and independent change in the optical properties of the LC layer corresponding to each pixel. The parallel aligned nematic liquid crystal molecules possess dielectric anisotropy. They show effective birefringence under an applied electric field. Applied voltage across the electrodes of a pixel changes the orientation angle of the liquid crystal molecules in the region with respect to director, leading to a phase retardation of the incident light in that region. Hence by controlling the voltages across each of the pixels, the phase of the light can be modulated independently. The SLM employed in our HOTS setup is driven through a DVI interface providing a 16-bit pixel data to the SLM, the 16-bit operation being supported by 24-bit 512×512 images transferred through an NVIDIA graphics card (Nvidia Quadro FX 580).

A photograph of the developed HOTS setup is shown in Figure 1(a). The HOTS set-up is designed around an inverted microscope (Olympus IX81). An Nd:YAG fiber-coupled, continuous-wave TEM00 laser ($\lambda=1064$ nm) beam is coupled to the microscope through a series of optical components. The schematic of the setup is shown in Figure 1(b). The laser beam is first passed through a set of polarizing optics to control the polarization and then expanded by a beam expander to fill the active area of SLM. The lenses L1, L2 and the microscope objective lens form two interconnected 4f imaging systems, making the relationship between SLM plane and the sample plane a simple Fourier transform. The diffracted beam reflected off the SLM is coupled to the high NA objective lens of microscope, which produces a tightly focused laser spot capable of trapping a multitude of submicroscopic particles in three dimensions.

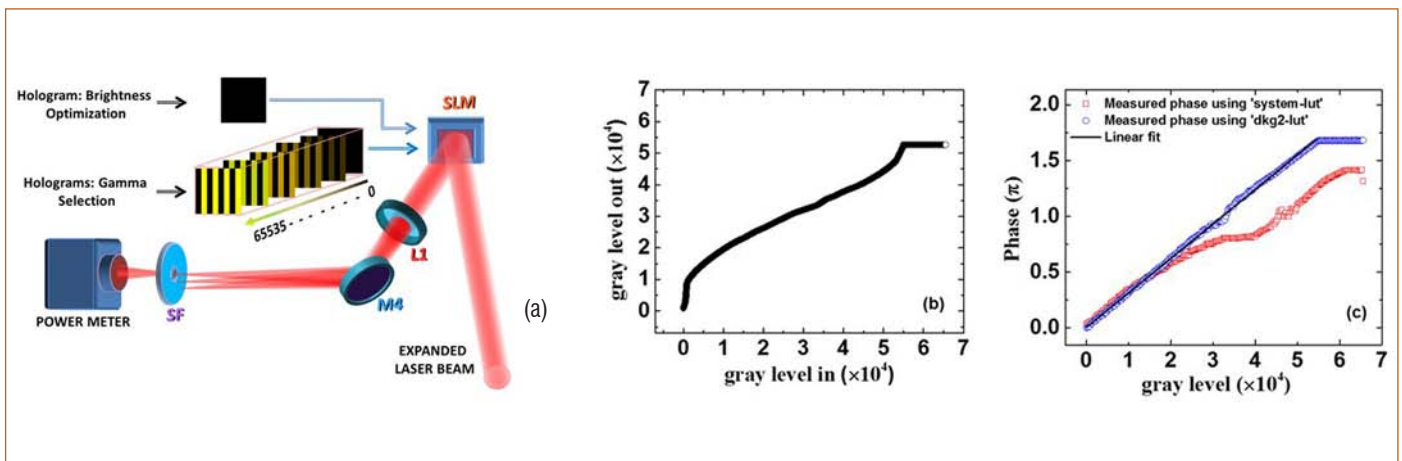


Figure 2: (a) Schematic of the setup to measure the first-order diffracted power (b) Plot of the phase compensation profile (termed dkg2-lut), (c) Plot of measured phase modulation curve (i) using system-lut (red circles) and (ii) using dkg2-lut (blue circles).

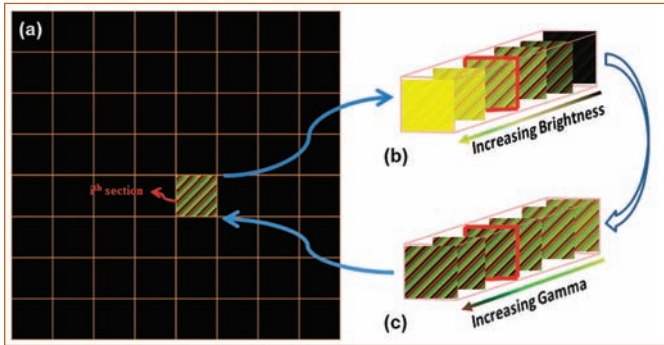


Figure 3: (a) Typical hologram divided into 64 subsections with the i th subsection with a blazed grating and the other subsections being kept blank, (b) Set of holograms with varying brightness/contrast levels and (c) Set of holograms with varying gamma levels.

Calibration of the SLM

Optimization of graphics card settings

The SLM used in the HOTs set-up is driven by a DVI interface. The holograms computed to produce the desired pattern at the sample plane are transferred through a graphics card to the SLM. The setting of the graphics card plays an important role in the first-order diffraction efficiency of the SLM and also in achieving uniformity in intensity among the trap spots. To optimize the graphics card settings, a method similar to the one used for computer monitors is used. This is implemented in experiments by a diffraction-based method as described in Figure 2(a). A power meter was placed on the Fourier plane of the SLM after the pinhole (SF) to measure the power of various orders diffracted off the SLM when different diffractive elements are imposed over it. To optimize the brightness

or black level, the contrast in the graphics card settings is set to its minimum value. Then a hologram representing a true black (i.e., a 16-bit depth image) having $[0,0,0]$ gray values all over its 512×512 pixels is displayed on the SLM, which is shown in Figure 2(a). The power of the first-order diffracted beam was measured as a function of the different brightness levels of the graphics. The minimum observed at a brightness level of 97%, represents the true black. Then, the contrast was set to its highest value of 100% to achieve maximum diffraction efficiency for the first-order diffracted beam.

To select a suitable gamma, a sequence of holograms with two phase levels, i.e., a linear binary diffraction grating with 50% duty cycle, was displayed on the SLM, keeping one of the phase levels constant at 0 and the other being stepped through a range of gray values starting from 0 to 65535, as shown in Figure 2(a). For each displayed hologram, the power of either of the $+1^{\text{st}}$ or -1^{st} -order diffracted beam was measured at the Fourier plane of the SLM. From the measured data, the location of the maxima corresponding to the phase modulation depth of π was identified. The value of gamma for which maximum power is obtained in the first-order diffracted beam is identified to be 0.66. This value of gamma places the first-order maximum (corresponding to the phase value of π) at the center of the available gray values, i.e., at 32,768, leading to uniformity in the resolution with which the gray levels are addressed in the range of 0 to π and π to 2π , i.e., a symmetric phase modulation depth on either side of gray value 32,768. All measurements were done with reference to a linear LUT.

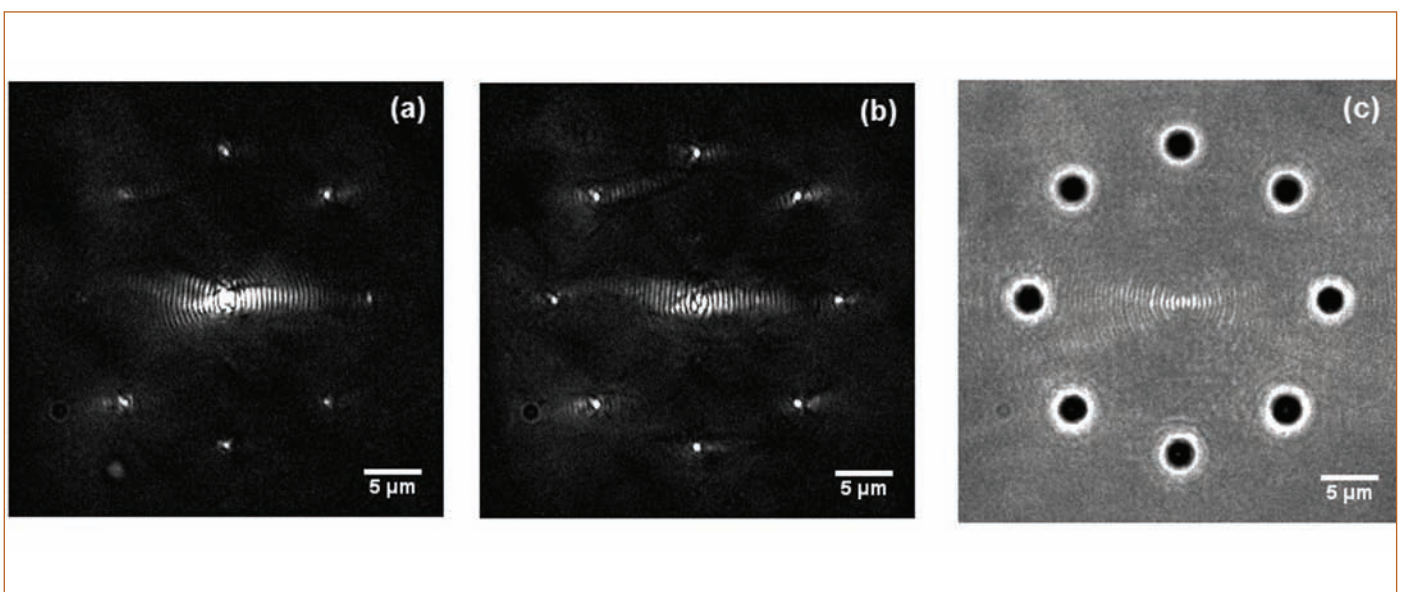


Figure 4: (a) Circular array of eight trap spots using system-lut, (b) using the developed dkg2-lut. (c) Polystyrene spheres of diameter $1.2 \mu\text{m}$ trapped in the array generated using an optimized hologram with SVPR correction and using dkg2-lut.

Two other parameters that affect the performance of an SLM, are digital vibrance (DV) and hue (H). The values of these parameters were set to 50% and 0° , respectively. The digital vibrance if set below and above 50% lead to the oscillation of the power levels with respect to the addressed gray values, leading to a loss of first-order diffraction efficiency. Similarly, the hue set at any angle above 0° also led to a decrease in first-order diffraction efficiency. The optimized graphics settings for the SLM with the NVIDIA graphics card used in our HOTs setup are $B = 97\%$, $C = 100\%$, $G = 0.66$, $DV = 50\%$, and $H = 0^\circ$.

Phase characterization and compensation of phase nonlinearity

A sequence of holograms with two phase levels, one fixed at 0 and the other stepped through the range of gray levels to be characterized, i.e., 0 to 65,535, realized as linear binary diffraction gratings with 50% duty cycle with a grating period of 16 pixels are displayed over the SLM. The power of the first-order diffracted beam (either of the first order) is measured using a power meter for each of the displayed holograms in the sequence. The measurements were done with a linear LUT. The phase modulation curve was extracted from the measured power levels as a function of grey level and a phase compensation profile (named dkg2-lut), which compensates for the nonlinearity in phase response was developed as shown in Figure 2(b). Figure 2(c) shows the phase modulation curve measured for the SLM (i) using the system-lut and (ii) using the generated LUT (dkg2-lut). It is clear from Figure 2(c) that the phase

modulation characterized using the system-lut shows a nonlinear phase response, whereas the one using dkg2-lut shows a linear phase response; a linear fit to the phase response curve is also shown. The phase compensation improved the phase modulation depth from 1.4π (using system-lut) to 1.67π (using dkg2-lut). It is found that the first-order diffraction efficiency improved to 50% by using dkg2-lut, as compared to the one measured using the system-lut, where the measured first-order diffraction efficiency was only 29%.

Calibration of the SLM for SVPR

The above-discussed phase compensation method compensates for the nonlinearity in phase response behavior of the SLM globally. The liquid crystal SLMs are known to differ in their phase response over different spatial regions of the SLM. A simple and robust technique for calibrating the varying phase response behavior over the spatial region of the SLM is presented. To characterize the local phase responses over the spatial region of the SLM, the SLM is divided into 8×8 subsections. A blazed grating is displayed on a subsection [Figure 3(a)], while the rest of the sub-sections are kept blank, and the resulting power at first-order diffraction spot at the Fourier plane of SLM is measured using the diffraction set-up [Figure 2(a)]. The holograms for each of the subsections are optimized sequentially for maximum power at the first-order diffracted beam by varying the brightness/contrast [Figure 3(b) and gamma [Figure 3(c)]. The procedure is repeated for each of the

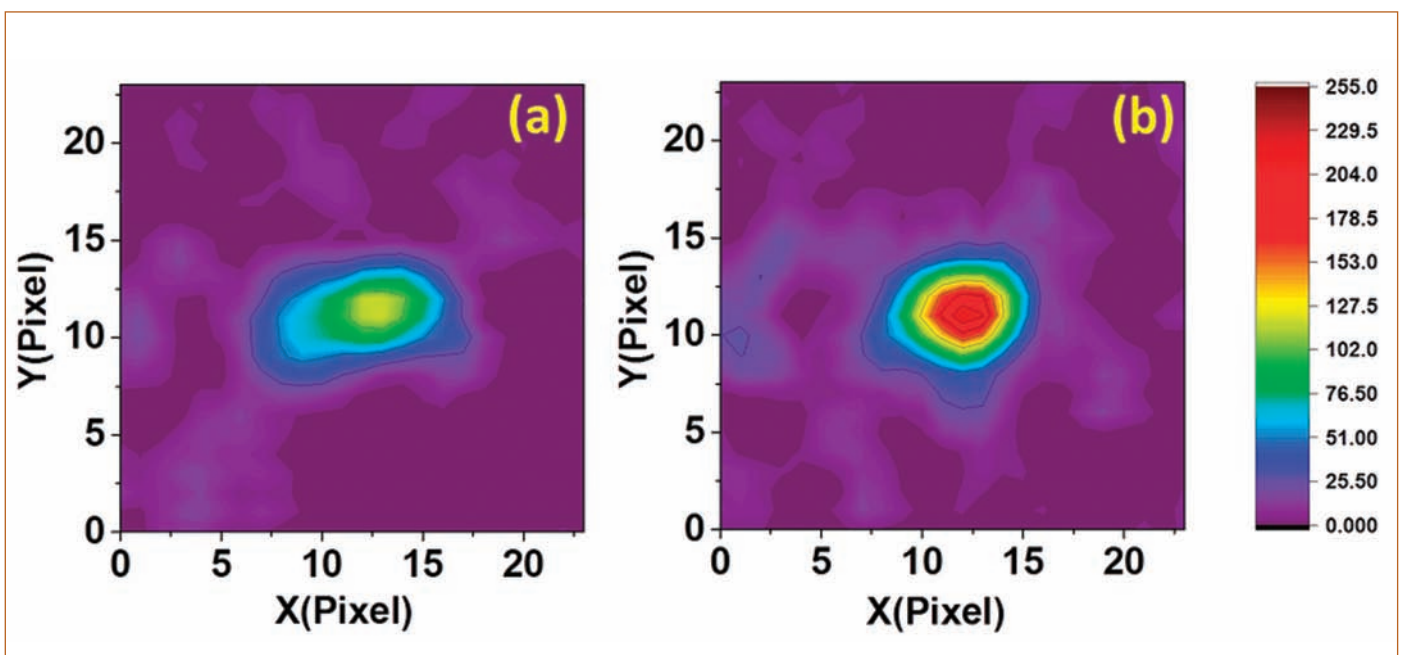


Figure 5: Intensity plot of a typical trap spot (a) before SVPR correction and (b) after SVPR correction.

subsections (64 subsections in our case) and the final hologram is the combination of optimized holograms from each of the subsections. It is found that with the above correction the first-order diffraction efficiency improved from 50% to 55%.

Array of holographic optical traps

To generate an array of traps, weighted Gerchberg Saxton (WGS) algorithm is used to generate the hologram to produce traps with theoretical uniformity (>99%). The generated hologram is displayed over SLM to produce the desired spots at the focal plane. An array of eight focal spots (Figure 4) in a circle was generated by displaying a suitable hologram on the SLM. Figure 4(a) shows the trap spots in a circle generated using system-lut. Non-uniformity in the intensities of the traps generated along with a strong zeroth-order beam are seen. Figure 4 (b) shows the same array of traps in a circle generated using the optimized LUT, dkg2-lut (corrected for SVPR). It is seen that the intensities of the trap spots are fairly uniform, with a less intense zeroth order, showing improved first-order diffraction efficiency. Uniformity in the intensities of the created trap spots is found to be improved from 76 to 97% with the optimized LUT with correction for SVPR compared to that generated using system-lut.

Moreover, all spots in the array in the circle as shown in Figure 4(a) were not able to trap the particles in a stable manner. Only a few spots were observed to trap the particles (Polystyrene, diameter 1.2 μm) along with a strong trapping in the zeroth-order spot, whereas all the trap spots created using the optimized hologram (Figure 4(b)) were capable of trapping particles, with no trapping at the zeroth-order spot. Figure 4(c) shows polystyrene spheres of diameter 1.2 μm , suspended in water trapped in the array of eight focal spots in a circle at a distance of 10 μm away from the coverslip, the trap spots being generated using the optimized hologram with dkg2-lut and SVPR correction. The average trap stiffness at all eight trapping sites is $1.26 \pm 0.16 \mu\text{N/m}$. The uniformity in trap stiffness is found to be 80%, limited by the phase modulation depth of 1.67π for our SLM.

To understand the effect of SVPR correction on trap quality, the spot

sharpness metric is calculated, which is defined as

$$M = \left(\sum_n I_n \right)^2 / \sum_n I_n^2 \quad (1)$$

where I_n is the intensity of the n^{th} pixel and n is the total number of pixels in a given area. Low value of M implies a more tightly focused spot and, hence, a better trap quality.

A circle of nine pixel diameter was chosen around each of the focal spots, with spot center coinciding with the center of the circle. The spot sharpness metric is calculated for the circular region surrounding each trap using Eq. (1). It is observed that the correction of SVPR leads to an improvement in trap quality up to 6.5%. Figure 5 shows the intensity plot of a trap spot before and after SVPR correction, showing an improved trap quality. Further, the trap performance metric (M_p), defined as the ratio of the trap stiffness before aberration correction to that after correction is calculated. It is such that the lower the value of M_p , better is the trap performance. In the present case, we found $M_p = 0.49$ for a trapped particle in a given trap spot, indicating improved trap performance after SVPR correction.

A holographic optical tweezers (HOTs) set-up has been designed and developed using a phase-only reflective spatial light modulator (SLM) driven by a digital video interface (DVI) graphics. A methodology is presented to optimize the SLM for nonlinearity in phase response globally and for differing phase response over different spatial regions. An improvement in diffraction efficiency of 55 from 29% was observed. Uniformity in the intensity of the traps is found to improve from 76 to 97% as observed from reflective measurements resulting in an improved trap stiffness. The SVPR correction is found to improve the trap quality by reducing aberration and hence an improved trap performance.

Reported by

Dr. Deepak K. Gupta

Materials Science Group

Young Researcher's FORUM

Magnetic Domain Structure and its Field Induced Dynamics in Polycrystalline Pure Iron and Steels studied using Magnetic Force Microscopy



Dr. J. Abuthahir obtained his Master's degree in Physics from the University of Madras, Chennai. He joined IGCAR as a Junior Research Fellow in July 2012 and pursued his Ph.D. from HBNI under the guidance of Dr. Anish Kumar, NDE Division, Metallurgy and Materials

Group. He successfully defended his doctoral thesis titled "Studies of magnetic field induced domain wall dynamics in polycrystalline iron and iron based alloys using magnetic force microscopy" in October 2018. Presently, he is an Assistant Professor in Government College of Engineering, Srirangam, Trichy.

Magnetic domains are regions in which the spontaneous magnetization is unidirectional. It is well governed by one of the fundamental laws of nature, (i.e.) minimum energy configuration of the system. The magnetic domain formation is based on the intrinsic magnetism to balance the following energy terms; exchange energy, magneto static energy, magneto crystalline anisotropy energy, magnetostriction and domain wall energy. The exchange energy is the interaction among the magnetic moments which favour the parallel arrangement of magnetic moments, basically quantum mechanical in nature. The magnetostatic energy is the principal driving force for magnetic domain formation in the system to reduce the stray field. The magnetic anisotropy energy is based on the easy magnetization axes for the crystal structure. The magnetostriction or magnetoelastic energy determines the shape and the size of the magnetic domains for the compressed or deformed system. The domain wall energy compensates the stray field energy by formation of the new magnetic domain walls. Hence, the final configuration of magnetic domain structure is

formed by minimizing energy from the overall energy contributions. Magnetic domain structure and various interaction of the energy terms are complicated and a prediction of the structure of domains in ferromagnetic materials is rather difficult to achieve. Hence, in order to understand magnetization behaviour in ferromagnetic materials, the direct visualization of magnetic domains is required.

The magnetic domain imaging techniques made it possible to access direct information about magnetization and anisotropy distributions as well as advance details about the micro-magnetization processes. Various techniques have been employed for the visualization of magnetic micro and nanostructures on the surface of ultra-thin films to the bulk materials. These techniques have their own advantages and limitations making them suitable for specific applications. A few of the frequently used techniques are magneto-optical Kerr microscopy, Bitter method, Scanning Electron Microscopy with Polarization Analysis, Lorentz Transmission Electron Microscopy and Magnetic Force Microscopy (MFM).

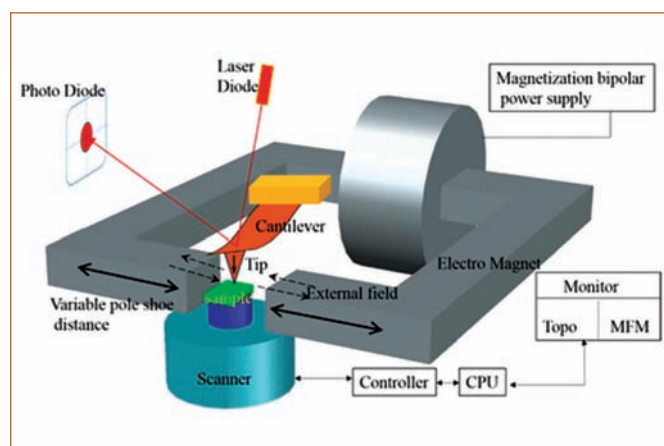


Figure 1: Schematic of the experimental setup for MFM imaging in presence of externally applied in-plane magnetic field.

MFM is an efficient tool in the characterization of magnetic microstructure at the surface of ferromagnetic materials at micro/nanoscale. MFM can image simultaneously the magnetic stray field of the surface and topography with the lateral resolution upto 10 – 15 nm with the scan size of around 100 μm . It can detect magnetic stray fields from the surface using a magnetically coated very sharp tip of the radius of curvature of about 20-40 nm. The long range magnetic interactions between specimen surface and a cantilever tip coated with magnetic material are less sensitive to topographic irregularities of the materials. Therefore, MFM requires minimal sample preparation and measurements are performed at ambient atmospheric conditions to obtain clear contrast of magnetic stray field images.

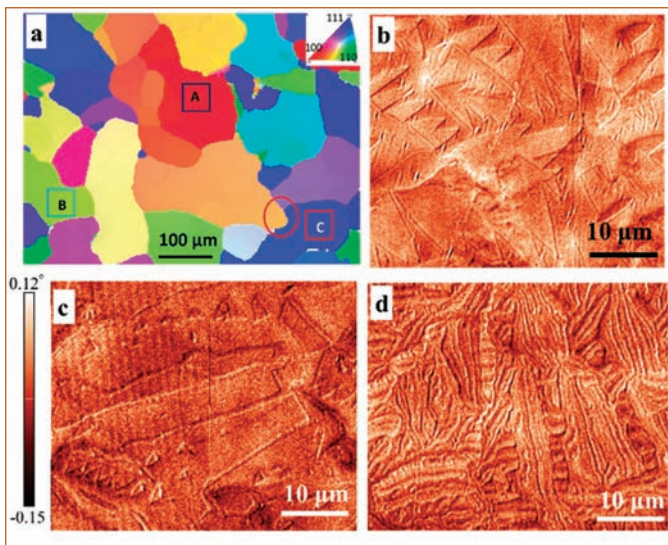


Figure 2: Inverse pole figure maps of the polycrystalline iron specimen in (a) Z_0 direction, MFM images obtained in grains with surface parallel to (b) $\{100\}$; (c) $\{110\}$; and (d) $\{111\}$. The grains are marked as A-C in (a), respectively.

Several studies have been reported on high resolution magnetic domain imaging in thin films and fabricated nanostructures. However, high resolution studies of magnetic domain structures in bulk polycrystalline samples are relatively less. Detailed characterization of magnetic microstructure in a bulk polycrystalline material can provide a better understanding of the micro-magnetization events, which is important for development of magnetic techniques for non-destructive characterization of the material. The present study demonstrates the applicability of MFM in combination with Electron Back-scatter Diffraction (EBSD) technique to study the influence of magneto crystalline anisotropy on the magnetic microstructure and field dependent domain wall dynamics on the surface of polycrystalline iron and iron based alloy steels.

Experimental Setup

The MFM experiments have been carried out using an NTEGRA AFM/MFM system supplied by M/s. NT-MDT. Co., Zelogonard, Russia. NOVA© software was used to perform data acquisition and analysis to obtain the topography and MFM phase images. The MFM instrument has the provision to perform field dependent domain wall dynamics in the presence of in-plane magnetic field in the range of ± 2000 Oe using the in-built electromagnet setup as shown in Figure 1. MFM studies in presence of high external magnetic field strength demand MFM tips to be coated with corresponding higher coercivity magnetic material to assure reliable magnetic imaging of the specimen surface.

The MFM cantilevers having spring constant of about 2-3 N/m and tips coated with high coercivity Co-alloy (~ 2 kOe) were used. The first free resonance frequencies were in the range of 60-65 kHz, the

tip radius was about 40 nm and the cantilever dimensions were $225 \times 35 \times 2.5 \mu\text{m}^3$, as mentioned by the manufacturer (NT-MDT).

Three specimens having ferromagnetic phases of different size, shape and volume fraction (viz) polycrystalline pure iron, duplex stainless steel (DSS) and cold worked AISI type 304 austenitic stainless steel (AUSS) are investigated. The chemical compositions of selected samples are given in Table.1.

Table 1: Chemical composition of the samples (wt%)							
Elements	Cr	Ni	Mn	Mo	Si	P	Fe
Pure Fe	-	-	-	-	-	-	99.99
DSS 2205	21.79	5.17	1.49	2.91	0.42	0.15	Bal
304 AUSS	18.32	9.26	1.63	0.25	0.35	0.34	Bal

Bulk Polycrystalline Iron

The influence of crystallographic orientation on the magnetic structure is studied in a polycrystalline iron specimen in the demagnetized state. The selected specimen was heat treated for 4 hours at 1373 K. The microstructure consists of an average grain size of $\sim 100 \mu\text{m}$. Figure 2a shows the EBSD inverse pole figure map for the surface normal direction of the sample (Z_0). MFM images provided the clear visualization of magnetic domains in the iron specimen with high lateral resolution of ~ 40 nm. A distinct variation in the domain structure is observed for the grains with different orientations. The grains with orientations close to $\{100\}$, $\{110\}$ and $\{111\}$ exhibited domains aligned in two perpendicular directions (Figure 2b), in one direction along $\{100\}$ (Figure 2c) and fine/ complex maze type domains, respectively. The domain structure are essentially influenced by the crystallographic orientation of the grain surface normal with respect to the cube axis i.e. the easy axis of magnetization.

A detailed analysis of the evolution of magnetic structure with applied field is studied in the region marked with circle in Figure 2a, which consists of three grains having distinct orientations. MFM

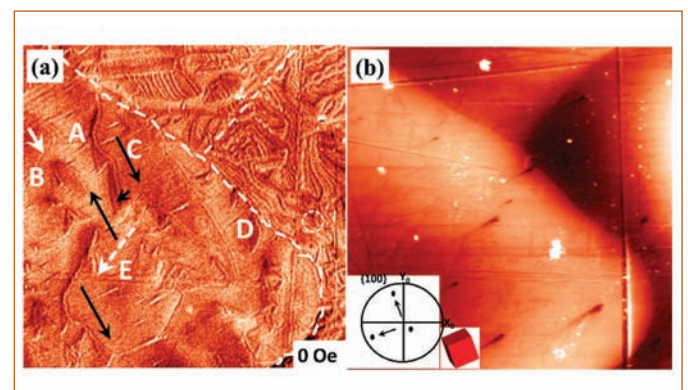


Figure 3: (a) MFM Phase map (b) Topography of the polycrystalline iron crystallographic orientation given in the inset of (b)

phase image and topography are shown in Figures 3a and b, respectively. MFM study with application of ± 2000 Oe external field demonstrated various micro-magnetization phenomena in the iron specimen. The domains with magnetization close to the field direction are found to grow at the expense of other domains having opposite magnetization direction.

Upon the application of external magnetic field, the pinning of domain walls at the surface defects were observed and the traces of a domain wall as a function of applied field were generated. Based on the bowing of a domain wall upon the application of external field (in Figure 4), the value of surface energy density of the domain wall is calculated as 52 mJm⁻².

Various micro-magnetization phenomena such as reversible and irreversible domain wall movements, expansion and contraction of

domains, Barkhausen jump, bowing of a pinned domain wall and nucleation of a spike domain could be visualized. The MFM studies in the presence of external field applied in two perpendicular directions are used to reveal the influence of the crystalline anisotropy on the local micro-magnetization.

Duplex stainless steel (DSS)

The duplex microstructure of DSS has almost equal amount of austenite phase in ferrite matrix. The MFM imaging clearly differentiates ferrite phase (ferromagnetic) from the austenite phase (paramagnetic) due to the maze type or complex stripe magnetic domains present in the ferrite phase. The microstructure of DSS helps us to study the influence of the interface (grain boundary) and the magneto crystalline anisotropic effect on the domain structure is discussed with the support of EBSD measurements (Figure 5a

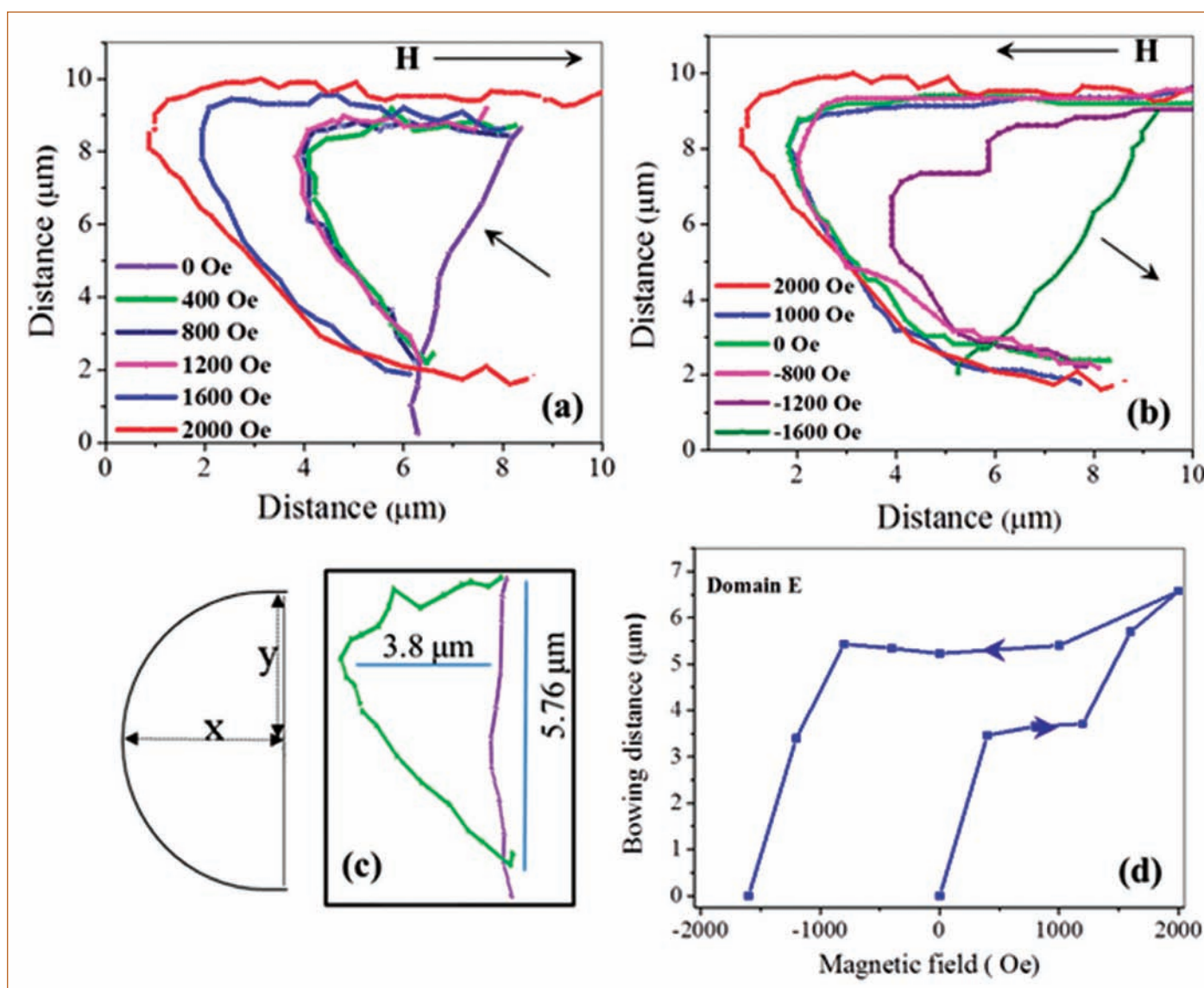


Figure 4: Trace of the bowing domain wall in domain E (shown in Figure 3a) during (a) increasing field from 0 to 2000 Oe and (b) decreasing field from 2000 Oe to -1600 Oe. The simplified schematic of the domain wall bowing defining the bowing distance (x) and distance between pinning points (2y) are shown in (c). (d) Shows the variations in bowing distance with applied magnetic field.

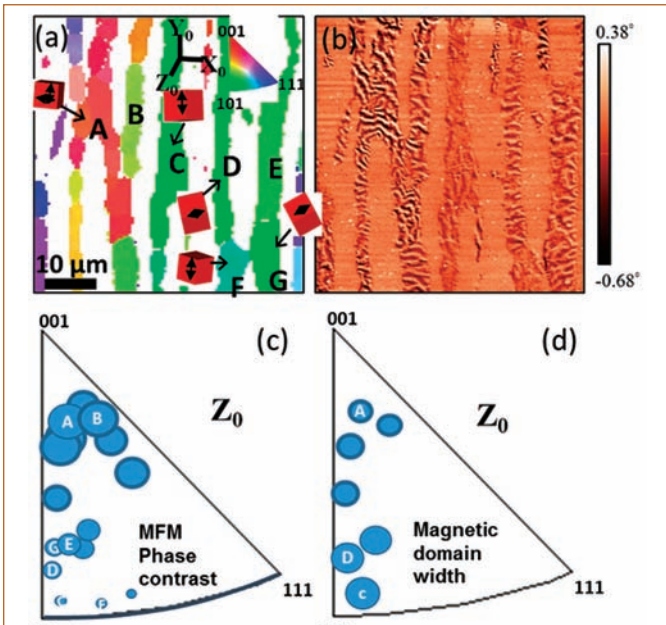


Figure 5: (a) IPF maps of the ferrite phase in surface normal (Z_0) direction and the respective MFM phase map. Influence of grain orientation on (a) maximum MFM phase contrast and (b) domain width. The size of the bubbles is proportional to the absolute values and the IPFs are shown corresponding to Z_0 direction.

and b). The width of the stripe domain increases linearly and the MFM phase contrast decreases almost linearly with the deviation of the surface normal from the easy axis ($\langle 100 \rangle$) of magnetization as depicted in Figure 5c and 5d.

MFM image of the same area as shown in Figure 5b was obtained in presence of in-plane external magnetic field in the complete cycle of ± 1600 Oe. The influence of applied field on the domain structure is analyzed in view of the direction of easy axis of magnetization on the surface with respect to the applied field.

In the range of applied magnetic field of ± 1600 Oe, no appreciable change in the domain structure is observed for the grains with plane normal close to $\langle 110 \rangle$ directions. However, alignment of the stripe domains in the direction of the applied field is clearly visualized for the grain with surface normal and applied field along $\langle 100 \rangle$ directions (in Figure 6).

The leakage of stray field at a grain boundary is found to appear at a threshold applied field perpendicular to the boundary and increases linearly with increasing applied field. Further, the stray field at a grain boundary is found to be the function of the mis-orientation between the adjoining grains and also depends upon the deviation of the surface normal from the easy axis of magnetization.

Cold Worked AISI 304 stainless steel

High resolution (30 nm) topography and MFM phase maps of a $10 \times 10 \mu\text{m}^2$ area obtained to clearly visualize the domain patterns in

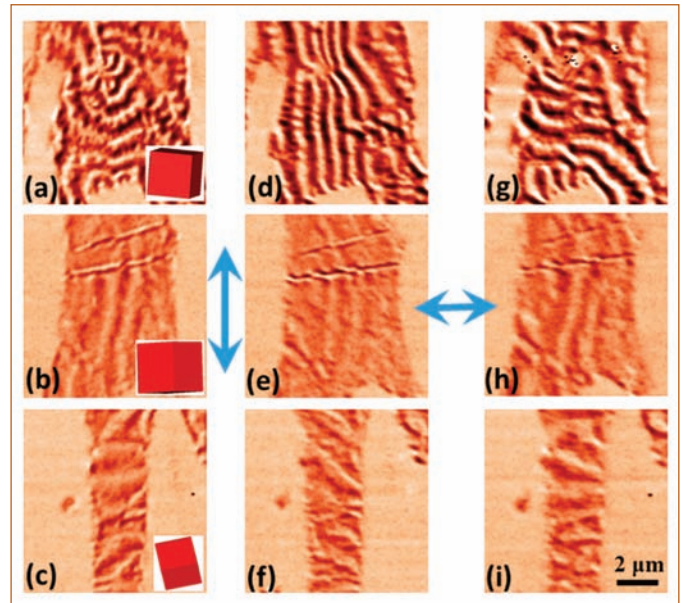


Figure 6: MFM phase maps for three grains with different crystallographic orientations (indicated in insets) at remnant conditions after applying magnetic cycles (± 1600 Oe) in the directions indicated by arrows.

α' -martensite phases are shown in Figure 7. Martensite phases of different shapes (round dots and lamellae of different thicknesses) and sizes can be observed in Figure 7b. MFM imaging could clearly identify the martensitic precipitates in the austenitic matrix due to the presence of magnetic domains leading to phase contrast in MFM imaging. The average area fraction of the martensite phase estimated by MFM imaging (22%) at different locations over the sample is found to be in good agreement with that obtained by X-ray diffraction technique (21%).

Both in-plane and out-of-plane magnetized domains have been observed for the precipitates with the same crystallographic orientations indicating strong effect of size or the shape anisotropy. The martensite precipitates having apparent circular shape with diameter smaller than $1 \mu\text{m}$ exhibited typical of single domain structures such as a vortex structure. The thin lamellae type α' -martensite precipitates (A and B indicated in Figure 7b) exhibit

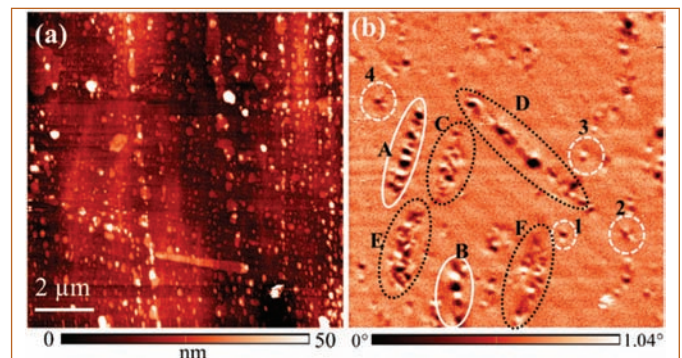


Figure 7: (a) Topography and (b) MFM phase map of 47 % cold worked AISI type 304 stainless steel.

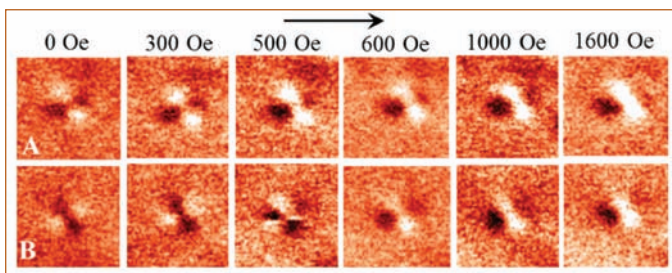


Figure 8: Rotation of two vortex domains (A and B) with opposite initial vortex directions with external field

perpendicular magnetization of the domain. The thick lamellae types (C-F indicated in Figure 6b) exhibited complex multi-domain structure with both in-plane and out-of-plane magnetization for the precipitates with the same crystallographic orientations indicating strong effect of size or the shape anisotropy. Micro-magnetization loops of two vortex domains with different initial orientations have also been studied (in Figure 8).

In summary, three specimens having ferromagnetic phases of different size, shape and volume fraction are investigated and their properties are shown in Figure 9. The study demonstrates applicability of MFM with EBSD for studying the crystallographic effect on the magnetic domain structures in the bulk polycrystalline

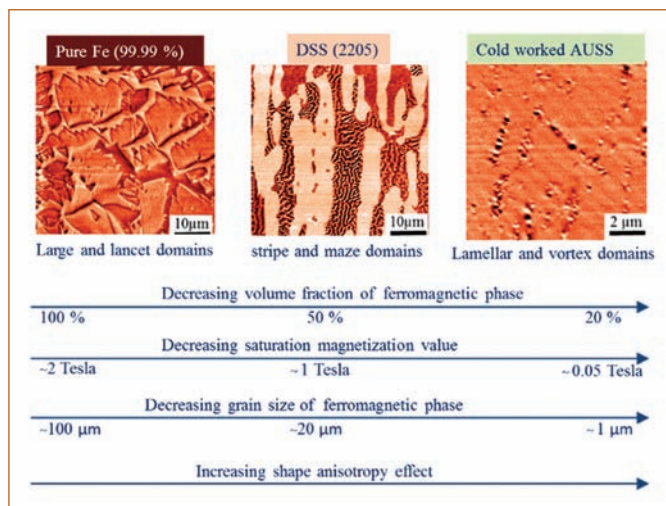


Figure 9: Comparison of microstructure and magnetic properties of materials studied.

materials. Shape anisotropy effect is more prominent with decreasing size of the ferromagnetic phase. MFM study in presence of external magnetic field provided clear visualization of various micro-magnetization phenomena which can be used for understanding the bulk magnetic properties.

*J Abuthahir
Metallurgy and Materials Group*

News and Events

A one day Security Sensitisation programme for Senior Officials of DAE units was conducted at IGCAR, Kalpakkam on 14.05.2019



Security Sensitisation programme



Special lecture by Sr. Prof. K. R. Munirathnam, WCSC, Chennai. on "Yoga for Harmonious Life".

On the occasion of 5th International Day of Yoga on 21.06.2019, Sr. Prof. K. R. Munirathnam, World Community Service Centre (WCSC), Chennai delivered a lecture on "Yoga for Harmonious Life" at Sarabhai Auditorium IGCAR, Kalpakkam. This was followed by a Practical Session on Yoga.

Foundation Day Celebration of IGCAR

April 30, 2019



From Left to right: Dr. S. A. V. Satya Murty, former Director IGCAR, Prof. P. R. Vasudeva Rao, former Director IGCAR & Vice Chancellor HBNI, Dr. Arun Kumar Bhaduri, Director IGCAR, Dr. R. Chidambaram, DAE-Homi Bhabha Chair Professor & Former Principal Scientific Advisor, Government of India, Shri K. N. Vyas, Secretary, DAE & Chairman, AEC, Shri S. K. Sharma, CMD, NPCIL, Dr. G. Amarendra, Chairman, Organising Committee and Director MSG & MMG, IGCAR

IGCAR celebrated its Foundation Day for the first time on April 30, 2019. It was this day in 1971 that Dr. Vikram Sarabhai, the then Chairman of the Atomic Energy Commission approved the formation of Reactor Research Centre (RRC) by an executive order, which was later renamed as Indira Gandhi Centre for Atomic Research in 1985.

The programme was conducted in a specially decorated pandal to seat about 1500 colleagues. Dr. R. Chidambaram, DAE-Homi Bhabha Chair Professor & Former Principal Scientific Advisor to Government of India was the Chief Guest of the event. Dr. Arun Kumar Bhaduri, Director, IGCAR welcomed the gathering. On this occasion, Shri K. N. Vyas, Secretary, DAE & Chairman, AEC presided over and inaugurated the 50th campaign of CORAL (COmpact Reprocessing facility for Advanced Fuels in Lead cells) facility. This has successfully demonstrated the feasibility of reprocessing high burnup mixed carbide fuel through successive campaigns over the years. A memoir cataloguing some of the major milestones of the Centre over the last forty eight years was released by the Guest of Honour, Shri S. K. Sharma, Chairman and Managing Director, NPCIL. The memoir also included rare photographs of noteworthy events of past, significant achievements in equipment design, distinguished visitors and former Directors and colleagues of the Centre, chronologically.

All former Directors and former Group Directors of the Centre were invited for the occasion. Former Directors of the Centre, Prof. P. R. Vasudeva Rao, Dr. S. A. V. Satya Murty and former Group Directors Shri G. R. Balasubramanian, Shri P. V. Kumar, Dr. R. Natarajan, Dr. D. V. Gopinath, Dr. L. V. Krishnan, Dr. A. R. Sundararajan, Shri R. D. Kale, Dr. G. Vaidyanathan,

Dr. P. Kalyanasundaram, Shri M. Rajan, Dr. K. K. Rajan, Shri S. A. Weling, Shri P. Sreenivasan, Shri Y. C. Manjunatha, Shri A. Jyothish Kumar, Dr. S. L. Mannan, Dr. K. Bhanu Sankara Rao, Shri M. P. Janawadkar, Shri P. V. Ramalingam, Shri G. Srinivasan, Dr. K. Nagarajan, Dr. M. Joseph, and Dr. C. S. Sundar attended and graced the occasion. All of them were honoured by Director, IGCAR with a shawl on the occasion.

Shri K. N. Vyas, Secretary, DAE & Chairman, AEC in his presidential address mentioned that IGCAR has established a comprehensive R&D facility covering the entire spectrum of FBR technology. He appreciated the Centre's focus on cutting edge field of fast reactor technology, which is very essential to India for guaranteeing future energy independence and to raise above rest of the world. He requested the younger colleagues to raise upto the challenges and put in best efforts to make fast reactor technology as safe and economical as possible. Chief Guest, Dr. R. Chidambaram, in his special address, highlighted the uniqueness of Kalpakkam in having various reactors fuelled by all the three isotopes, (viz.) Uranium 235(MAPS-NPCIL), Plutonium 239(FBTR-IGCAR) and Uranium 233(KAMINI-IGCAR). He emphasized that nuclear energy is a near renewable source of energy because of breeding and IGCAR plays a vital role in this mission and is hence a "Pride of the Country".

Towards encouraging younger colleagues to pursue higher studies and update their knowledge, Homi Bhabha National Institute (HBNI) started its academic programmes in the year 2006. The strength of the research scholars in the Centre has been steadily increasing over the years from fifteen to a present sanctioned strength of two hundred. During 2018 about 33 Scholars have completed their Ph.D. Programmes, 30 have received their M.Tech. degrees and 14 Scholars have been awarded their M.Sc. Engineering degrees. IGCAR has instituted awards for Best Thesis and Certificate of Appreciation to encourage younger colleagues and Research Scholars. A dedicated senior selection committee had looked into the research



Remote inauguration of 50th campaign of CORAL facility by Shri K. N. Vyas, Secretary, DAE & Chairman AEC, in the presence of Dr. R. Chidambaram, DAE- Homi Bhabha Chair Professor & Former Principal Scientific Advisor, Government of India, Dr. Arun Kumar Bhaduri, Director IGCAR and other dignitaries.



Special invitees

work of all the scholars, who had obtained their degrees during 2018. It identified the best performers in Physical, Chemical and Engineering Sciences streams. Totally twelve Research Scholars were selected and they received the awards during the function.

Gamma chamber facility at IGCAR is used for irradiation of seeds and plants such as Causurina, Crossandra or Kanagambaram, Guava and Chilli for enhancing their yield. It was a joyous moment when the saplings of “Kanagambaram”, which were a product of this irradiation facility, were presented to the Chief Guest, Guest-of-Honor and Chairman on this day by the Director, IGCAR. The programme concluded with a vote of thanks by Dr.G.Amarendra, Chairman Organising Committee. The dignitaries then visited various facilities in IGCAR including the construction site of FRFCF.

As a part of the foundation day celebrations, “Open House” was organized for families of employees of IGCAR. The event was conducted in two phases, on May 4 and May 11, 2019 (Saturdays) and the laboratories organizing visits were split into two groups, according to the number of employees and dependants to have roughly the same load of visitors on each day for better logistics. The visitors could see the Fast Breeder Test Reactor and also were shown a short film on its operations. The visitors were also shown various experimental facilities set up in different Groups of IGCAR, which are very unique and important. The open house was well attended and appreciated. Owing to popular demand from the employees of GSO, it was repeated on May 18, 2019 exclusively for the benefit of employees and family members of GSO. The Open House facilitating exposure to advanced experimental facilities is sure to motivate and inspire young children/students of the employees to take up scientific career in future. Totally around 1650 persons visited the Centre during this event.

Reported by

Dr. G. Amarendra, Chairman, Organising Committee

Open House Photo Gallery



Shake Table Facility at Reactor Design Group



FBTR- Inside Reactor Containment Building



FBTR - Control Room



Computer Lab, Electronics & Instrumentation Group



Concrete Lab, Engineering Services Group

Conference and Meeting Highlights

Dr. Baldev Raj Memorial Bridge Course on Non-destructive Evaluation and Quality Assurance (BRM-BCNQ)

IGCAR, Kalpakkam, May 20- 24, 2019



Inauguration of BRM-BCNQ 2019 by Dr. G. Amarendra, Director, MMG & MSG, IGCAR.

Dr. Baldev Raj Memorial Bridge Course on Non-Destructive Evaluation (NDE) and Quality Assurance (QA) (BRM-BCNQ 2019) was organised jointly by IGCAR, Indian Society for Nondestructive Testing (ISNT) Kalpakkam Chapter and Society for Failure Analysis (SFA) Chennai Chapter at IGCAR during May 20-24, 2019 for the benefit of students entering final year of B.E./ B.Tech/ M.E./ M.Tech (Mechanical/ Metallurgy/ Materials Science/ Industrial/ Manufacturing/ Production/ NDT/ Welding Technology) and young engineers. The objective of this unique course is to motivate young students by introducing advanced NDE science and technologies through a series of technical lectures by eminent experts and providing practical hands-on, in the state-of-the-art NDE equipments. This course was attended by 34 participants that include 18 motivated students from academic institutes and 16 engineers from IGCAR.

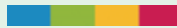
Dr. G. Amarendra, Director, MMG & MSG, IGCAR inaugurated the course on May 20, 2019. During his address, he highlighted the role of NDE and QA in nuclear industry and encouraged the students to learn as much as possible during this unique course. A special address was given by Dr. A. Ravisankar, the then Director, RpG & Project Director, Fast Reactor Fuel Cycle Facility (FRFCF), IGCAR highlighting the importance of this course and motivating the students to learn towards safe operation & effective maintenance of engineering components. Dr. B. P. C. Rao, Associate Director, FRFCF and Chairman, BRM-BCNQ 2019 briefed the importance of the Bridge Course and career in NDE and recalled his association with Late Padma Shri Dr. Baldev Raj, who initiated and nurtured NDE and QA fraternity in India and particularly at IGCAR.

Expert faculty from IGCAR delivered technical lectures covering various advanced NDE and QA techniques including failure analysis. The lectures were well received and the participants interacted very well with the faculty. During the afternoon sessions, participants performed mini-project to gain hands-on experience in advanced NDE equipments. The participants visited FBTR to get familiarized with the nuclear plant. A quiz competition was conducted on May 24, 2019. Dr. C. K. Mukhopadhyay, Head, NDE Division and Convener, BRM-BCNQ 2019 delivered the vote of thanks. During the feedback session on May 24, 2019, the students lauded the bridge course and mentioned that they were immensely benefitted by attending the course. They expressed that the course was well structured and executed and thanked the organisers for the rare opportunity provided to them. All the students were given participation certificates. The winner and runner teams of the quiz competition were also given certificates.

Reported by

Dr. C. K. Mukhopadhyay, Convener, BRM-BCNQ 2019

Conference and Meeting Highlights



One day Training Programme on “Nuclear Radiation in Fuel Cycle”

May 21, 2019



Release of handout by Dr. A. Ravisankar, the then Project Director, FRFCF during the Inaugural Function



Presentation by one of the speakers during the programme

A one day training programme on “Nuclear Radiation in Fuel Cycle” was organised on May 21, 2019 in FRFCF. Dr. B. P. C. Rao, Associate Director, FRFCF welcomed the participants and briefed about the genesis and structure of the programme. He highlighted the importance of acquiring knowledge on radiation, as FRFCF will be soon taking up pre-commissioning activities after completion of construction of the 5 plants in the nuclear island. Dr. A. Ravisankar, the then Project Director, FRFCF inaugurated the programme and in his address emphasised the importance of this programme at this juncture, considering the type and nature of fuel being handled in FRFCF. He narrated his hands-on experiences on radiation during the construction and operation of CORAL and DFRP and highlighted the challenges of remotisation, shielding, and O&M. He reiterated the need for adhering to the safe practices developed over the years at IGCAR. Dr. B. Venkatraman, Director, SQRMG and ESG addressed the gathering. He stressed the need for better understanding of nuclear radiation for safe work and quality output. He advised them not to fear about the radiation, but to learn from the expert lectures being delivered by the experienced faculty in this programme, so that they can handle radiation with confidence. Dr. M. T. Jose, Convener thanked the dignitaries.

The programme covered topics from basics of nuclear radiation to emergency preparedness and criticality safety. The basics of radiation physics was explained by Dr. O. Annalakshmi. Mrs. R. Akila covered the topics on radiation monitoring in reprocessing plants. The biological effects of radiation were brought out by Dr. R. Sarangapani, SQRMG. Dr. R. V. Subba Rao, Head, PRCD, RpG delivered a talk on accounting of nuclear materials. Later, radiation safety and criticality safety aspects were covered by Shri R. Santhanam and Shri S. Chandrasekharan from SQRMG respectively. The concluding talk on emergency preparedness was given by Dr. M. T. Jose. More than 50 participants attended and interacted with the speakers. In the feedback session, they indicated that the talks and the hand-outs were very informative and useful.

*Reported by
Dr. M. T. Jose, Head, IFS, FRFCF*

HBNI-IGCAR Corner

Awards received during IGCAR Foundation Day celebration, IGCAR, April 30, 2019.

Ph.D.

Best Thesis:

- Dr. K. A. Irshad: "Studies on Crystal Structure of Functional Rare Earth Sesquioxides at High Pressures".
- Dr. K. Chinaraga Pitchaiah: "Solubility studies on ligands in supercritical carbon dioxide medium and their application to extraction of actinides"
- Dr. Vikas Kumar: "Development of weld pattern analyzer for quality analysis of Arc Welding Process"

Certificate of Appreciation:

- Dr. L. K. Preethi: "Band Gap Engineering of Titania Nanotubes for Photocatalytic water splitting to generate Hydrogen".
- Dr. D. Sanjay Kumar: "Studies on some novel methods of synthesis and sintering of nanocrystalline ceramics".
- Dr. Sambasiva Rao: "Studies on development of a pulsed eddy current system for testing thick stainless steel components"

M.Sc. (Engineering)

Best Thesis:

- Shri Avinash Kumar Acharya: "Development of imaging technique for depiction of molten fuel coolant interaction process"

Certificate of Appreciation:

- Ms. S. Rajeswari: "Development of a web based OCR for text extraction and processing from scanned documents"

M. Tech.

Best Thesis:

- Shri Altaf Ali: "Study on ultrasonic technique as an alternative technique to radiography for inspection of PFBR blanket pins end plug welds".

Certificate of Appreciation:

- Shri Ritesh Singh: "Design and development of a system to localise a fuel subassembly with a failed fuel pin at dry rupture stage".
- Shri Ashish Kumar: "Mechanical Design of Sweep Arm Scanner for Scanning Fast Breeder Reactor Core".
- Ms. Gargi Panda: "Indigenous development of prototype over-current protection numerical relay".

HBNI-IGCAR Corner

Awards received during HBNI Foundation day celebration, HBNI-Mumbai, June 03, 2019:

Ph. D. :

Dr. Subrata Ghosh: “Vertical Graphene Nanosheets: Growth, Structure and Electrochemical Performance”.

Dr. A. K. Sivadasan: “Optical Properties of AlGaN Nanostructures”.

Dr. Vikas Kumar: “Development of Weld pattern Analyser for Quality Analysis of Arc Welding Process”.

M. Tech:

Ms. Shobhna Mishra: “Study of Electromagnetic Expansion Welding of Aluminium Alloy Tube to Aluminium Alloy Flange at Different Energy Levels and Weld Characterisation”.

M.Sc. (Engineering) :

Shri T. Suresh Kumar: “Isothermal low cycle fatigue evaluation of 316 LN austenitic stainless steel weld joint in aged and unaged conditions”.

Ph.D Thesis Defense

Name	Title	Date	Discipline
Mr. J. Christopher	Internal-State-Variable Based constitutive modeling and its Applicability to Tensile and Creep deformation of Tempered Martensitic 9% Chromium Steels	26.04.2019	Engineering Sciences
Ms. S. Prema	Development of Solution-focused Automatic Parallelization Mechanism with Tools and Techniques	04.05.2019	Engineering Sciences
Mr. Niranjan Kumar Pandey	Studies in the Mass Transfer with Chemical Reactions for Liquid-Liquid and Gas-Liquid-Solid Systems in Nuclear Industry	06.05.2019	Engineering Sciences
Mr. Manoj Kumar Parida	Design of solid state neutron detectors using GEANT4 simulation	24.05.2019	Engineering Sciences
Mr. Santosh Kumar	Hot Deformation Behavior of AISI Type 316 LN Austenitic Stainless Steel	12.06.2019	Engineering Sciences
Ms. P. C. Clinsha	Studies on Synthesis, Characterization of $\text{AgI}_{(1-x)}\text{Cl}_{(x)}$ Solid Solutions for I_2 & Cl_2 Sensing Properties	02-05-2019	Chemical Sciences
Mr. Debasish Saha	Studies on the Production, Separation and Purification of Carrier Free Radioisotope, ^{89}Sr using Yttria Target in Fast Breeder Test Reactor (FBTR)	03-06-2019	Chemical Sciences

Awards and Honours

Awards and Honours

Department of Atomic Energy had instituted “Swachhta Pakhwada Awards” to the constituent units of DAE for the exemplary performance during the Pakhwada. Indira Gandhi Centre for Atomic Research was awarded the Certificate of Excellence (second position among the DAE units) for its Swachhta activities (February 16-28, 2019). IGCAR has bagged this award second year in succession.

Dr. Aritra Sarkar was awarded **Alexander von Humboldt Fellowship** for Postdoctoral research by AvH foundation, Germany April-2019

Best paper/Poster Awards

Thermal conductivity enhancement of an organic phase change material using carbon black and nickel nanoinclusions for latent heat thermal energy storage applications.

Amit Kumar Mishra, B. B. Lahiri and John Philip

International Conference on Advanced Materials (ICAM 2019) held during June 12-14, 2019 at Nirmalagiri College, Kannur Kerala.

Best Paper Award

Biodiversity Basket - Avian Fauna



Golden Oriole

Indian Golden Orioles are medium-sized birds and winter migrants to southern parts of India. Both male and female are similar in size but different in colors.

Editorial Committee Members: Dr. T. S. Lakshmi Narasimhan, Dr. N. V. Chandra Shekar, Dr. C. K. Mukhopadhyay, Dr. Vidya Sundararajan, Shri A. Suriyanarayanan, Dr. C. V. S. Brahmananda Rao, Dr. V. Subramanian, Ms. R. Preetha, Shri J. Kodandaraman, Shri G. Venkat Kishore, Shri S. Kishore, Dr. N. Desigan, Shri M. Rajendra Kumar, Shri V. Rajendran, Ms. S. Rajeswari, Shri K. Ganesan, Shri K. Varathan and Shri G. Pentaiah